Atomistic spin simulations of electric-field-assisted nucleation and annihilation of magnetic skyrmions in Pd/Fe/Ir(111)

Moritz A. Goerzen [1,*] Stephan von Malottki [1,2,3] Grzegorz J. Kwiatkowski [2] Pavel F. Bessarab [2,4,5] and Stefan Heinze [1,6]

[1]*Institute of Theoretical Physics and Astrophysics, University of Kiel, Leibnizstrasse 15, 24098 Kiel, Germany*
[2]*Science Institute of the University of Iceland, 107 Reykjavík, Iceland*
[3]*Dartmouth College, Thayer School of Engineering, Hanover, New Hampshire 03755, USA*
[4]*ITMO University, 197101 St. Petersburg, Russia*
[5]*School of Science and Technology, Örebro University, Fakultetsgatan 1, SE-70281 Örebro, Sweden*
[6]*Kiel Nano, Surface, and Interface Science (KiNSIS), University of Kiel 24098, Germany*

We provide a theoretical background for electric-field-assisted thermally activated writing and deleting of magnetic skyrmions in ultrathin transition-metal films. We apply an atomistic spin model, which includes the exchange interaction, the Dzyaloshinskii-Moriya interaction, and the magnetocrystalline anisotropy energy. The strengths of the magnetic interactions are taken from density functional theory (DFT) calculations for a Pd/Fe bilayer on the Ir(111) surface. We systematically vary all magnetic interactions up to ±10% treating the magnetoelectric effect in linear response. The critical magnetic fields marking the onset of the skyrmion phase and the field-polarized phase shift considerably upon varying the interaction constants due to the electric field. Based on harmonic transition state theory, we calculate the transition rates for skyrmion nucleation and annihilation, which are in good agreement with experimental values for Pd/Fe/Ir(111). The field-dependent variation of energy barriers and preexponential factors leads to large changes of the transition rates, which are accompanied by changes in skyrmion radii. Finally, we simulate the electric-field-dependent writing and deleting of magnetic skyrmions in Pd/Fe/Ir(111) based on the master equation and transition rates obtained using the magnetic interactions calculated via DFT for electric fields of $\mathcal{E} = \pm0.5$ V/Å. The magnetic-field-dependent skyrmion probability follows a Fermi-Dirac distribution function of the free energy difference of the skyrmion state and the ferromagnetic (FM) state. The probability function for the opposite electric field directions is in striking agreement with experimental results [Romming *et al.*, Science **341**, 636 (2013)].

I. INTRODUCTION

Since their discovery [1–4] magnetic skyrmions [5,6] are subject of intense research due to their promising properties for future information technologies such as probabilistic computing [7,8], neuromorphic computing [8,9], racetrack data storage [10–12], or logic devices [13]. Key properties of skyrmions for applications are their nanoscale size [4,14,15], manipulation by electric currents [10,16], and an integer topological charge [6,16], leading to enhanced stability [17]. Since the topological protection is not strict for materials consisting of localised atomic magnetic moments on a discrete lattice [18], a continuous transition between states of different topological charges with a finite energy barrier exists.

The finite activation energy gives rise to the possibility of nucleating and annihilating skyrmions. Such a transition, which changes the topological charge can be triggered by spin-transfer or spin-orbit torques [4,19,20]. However, current-induced approaches suffer from an increase in temperature due to Joule heating and consequently decrease the

average lifetime of skyrmions, the temperature dependence of which is often described by an Arrhenius law [12,21–31]. A promising energy efficient approach for skyrmion-based devices, which avoids the Joule heating problem is the use of electric fields, which have the additional advantage that they can be applied locally. Electric-field-induced writing and deleting of magnetic skyrmions have been demonstrated experimentally [32,33]. However, the underlying microscopic mechanism of these phenomena is still a matter of debate.

Applying an electric field perpendicular to the surface of a metallic film will act on the magnetic interactions due to the magnetoelectric- and Rashba effect [34–40]. As a result the energy and entropy of states will be influenced, making either nucleation or annihilation processes more likely to occur. This consequently enables a transition by thermal noise or, at least, lowers the necessary amount of energy needed for a triggered transition.

Here, we demonstrate by means of atomistic spin simulations the concept of electric-field-assisted thermally activated nucleation and annihilation of magnetic skyrmions, which can be realized e.g. by hot electron injection in the setup of a scanning tunneling microscopy (STM) experiment. We focus on the well-studied system of a Pd/Fe bilayer on the

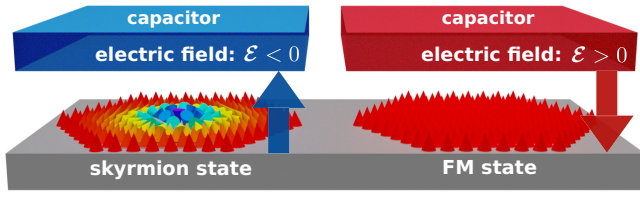*Corresponding author: goerzen@physik.uni-kiel.de

FIG. 1. Model for the influence of electric fields on the lifetimes of magnetic states at an interface. The homogeneous electric field, assumed to be generated in a plate capacitor geometry, changes the magnetic interactions due to spin dependent screening of the field by the electrons. This variation can either favor the skyrmion or the FM state, which allows electric-field-assisted thermally activated nucleation or annihilation of skyrmions.

Ir(111) surface for which writing and deleting of individual skyrmions via STM has been achieved [4]. We apply an atomistic spin model with all magnetic interaction constants obtained from density functional theory (DFT), which leads to a good agreement with experimental data on the magnetic phase diagram and switching rates for skyrmion creation and collapse [25,41–43]. The atomistic spin model allows to include frustrated exchange interactions in our simulations, which has recently also been achieved in micromagnetic simulations [44,45]. We assume a homogeneous electric field in the tunnel junction as in a plate capacitor (Fig. 1) and a linear dependence of the magnetic interaction constants with the field strength.

In the first part of our study, we systematically vary the strengths of the exchange interaction, the Dzyaloshinskii-Moriya interaction (DMI), and the magnetocrystalline anisotropy energy (MAE). We calculate the creation and annihilation rates within the harmonic approximation of transition state theory. The obtained rates are in good agreement with experimental STM data for Pd/Fe/Ir(111) [20]. Upon electric-field-induced variation of the magnetic interaction strengths we find significant changes of the critical magnetic field between the skyrmion and the field-polarized phase and of the transition rates.

In the second part of our article, we show that the variation of the transition rates enables electric-field-assisted thermally activated writing and deleting of magnetic skyrmions. Based on the master equation, we calculate the probability of finding a skyrmion as a function of the external magnetic field for electric field values of $\mathcal{E} = \pm 0.5$ V/Å. The changes of the magnetic interactions due to the electric field are obtained from DFT calculations for Pd/Fe/Ir(111), which show that the exchange interaction is most significantly affected, while the DMI and MAE vary much less. The calculated skyrmion probability as a function of the magnetic field resembles a Fermi-Dirac distribution function and is in remarkable agreement with experimental data of Romming *et al.* [4]. We further show that the Fermi-Dirac distribution, defined as a function of the free energy difference of skyrmion and FM state, can be shifted with respect to the magnetic field by an applied electric field, consequently increasing or decreasing the skyrmion probability.

This article is structured as follows. In Sec. II we introduce the atomistic spin model including the effect of an electric

field. We further describe how the transition rates are obtained using the geodesic nudged elastic band (GNEB) method and harmonic transition state theory. In the first part of Sec. III, we show systematically how a variation of the magnetic interaction constants affects the properties of spin spirals, zero-field magnetic phase diagrams, as well as skyrmion annihilation and creation rates. In the second part of Sec. III, we demonstrate that the transition rates obtained from our spin model with DFT-calculated parameters reproduce experimental STM data [20]. Finally, we solve the master equations using the transition rates calculated for DFT interaction constants of Pd/Fe/Ir(111) at electric field values of $\mathcal{E} = \pm 0.5$ V/Å. The obtained skyrmion probability as a function of magnetic field is compared with available experimental data of Ref. [4].

II. METHODS AND COMPUTATIONAL DETAILS

A. Atomistic spin model

We use a classical atomistic spin model to describe the magnetic interactions and the energy of an ultrathin transition-metal film. This extended Heisenberg model is given by

$$E = -\sum_{i,j} J_{ij}(\mathbf{m}_i \cdot \mathbf{m}_j) - \sum_{i,j} \mathbf{D}_{ij} \cdot (\mathbf{m}_i \times \mathbf{m}_j)$$
$$- \sum_i K(\mathbf{m}_i \cdot \hat{\mathbf{e}}_\perp)^2 - \sum_i M(\mathbf{m}_i \cdot \mathcal{B}_{\text{ext}}). \quad (1)$$

Here, the strength of the exchange interaction between pairs of normalized magnetic moments $\mathbf{m}_i$ and $\mathbf{m}_j$ at lattice sites i and j is given by the exchange constants J_{ij} and the DMI by the vectors $\mathbf{D}_{ij} = D_{ij}(\hat{\mathbf{z}} \times \mathbf{r}_{ij})$. M denotes the size of the magnetic moment at every site. The spins at every lattice site are subject to an uniaxial MAE contained in the constant K and to an external magnetic field $\mathcal{B}_{\text{ext}}$. In this study, the magnetic field is always pointing perpendicular to the surface.

In order to perform simulations for the model system of a Pd/Fe bilayer on the Ir(111) surface [4,20,25,26,41,46], all parameters in Eq. (1) are chosen from DFT calculations as given in Ref. [41]. As mentioned in the introduction, the application of an electric field leads to a spin-dependent screening by the electron density at the surface, which changes the magnetic interactions. Motivated by results from DFT [34,36,37,40,47] we model the influence of the electric field in linear response to the magnetic interactions.

To allow a systematic study of the effect of the electric field on the different interactions, we modify the MAE constant K as well as the nearest-neighbor exchange interaction and DMI, i.e., only J_1 and D_1 are varied. Thus in our model an electric field $\mathcal{E}$ perpendicular to the surface acts on the parameters $P = J_1, D_1, K$ according to $P' = P + \frac{\partial P}{\partial \mathcal{E}}\mathcal{E}$. For our systematic study we therefore define the relative deviations of magnetic interaction parameters

$$\delta J_1 = \frac{J_1' - J_1}{J_1}, \quad \delta D_1 = \frac{D_1' - D_1}{D_1}, \quad \delta K = \frac{K' - K}{K}.$$

Starting from the magnetic interactions for Pd/Fe/Ir(111) from DFT as given in Appendix A, the influence of a relative deviation of $-0.1 \leqslant \delta J_1, \delta D_1, \delta K \leqslant 0.1$, i.e., up to $\pm 10\%$ variation of the magnetic interactions, on the energy of

noncollinear magnetic states such as spin spirals and skyrmions with respect to the FM state is analysed.

In the final part of our study, we choose the changes of the interaction constants given by $\partial P/\partial \mathcal{E}$ using the DFT values calculated for Pd/Fe/Ir(111) [47]. Since the exchange interaction is most influenced in that system, we focus on the variation $\partial J_1/\partial \mathcal{E}$ obtained from DFT calculations for field values of $\mathcal{E} = \pm 0.5$ V/Å and neglect the variation of DMI and MAE.

For finding the required local energy minimum states, we performed atomistic spin dynamics simulations. In particular, the damped Landau-Lifschitz equation is iteratively solved for an initial spin configuration using an SIB solver [48]. For all spin dynamics simulations we used a damping parameter of $\lambda = 0.5$ and a system size of 200×200 atoms on a hexagonal lattice with periodic boundary conditions.

B. Harmonic transition state theory

The rates for annihilation and nucleation of magnetic skyrmions are calculated in the framework of transition state theory in harmonic approximation to the energy (HTST) [12,14,21,22]. Here, the transition rate $\Gamma^{A \to B}$ and the lifetime τ_A of an initial state A, e.g., a skyrmion, with respect to the transition to a state B, e.g., the FM state, are described by an Arrhenius law

$$\tau_A^{-1} = \Gamma^{A \to B} = \Gamma_0^{A \to B} \exp(-\beta \Delta E^{A \to B}), \qquad (2)$$

where $\beta = (k_B T)^{-1}$, $\Gamma_0^{A \to B}$ denotes the preexponential factor and $\Delta E^{A \to B}$ is the energy barrier between the two local energy minima.

In order to find the minimum energy path (MEP) for a transition between states and thereby the energy barrier we use the GNEB method [49,50]. By precisely locating the highest energy state along the MEP using the climbing image (CI), we find the saddle point (SP) defining the bottleneck for the A $\to$ B process—the transition state [49]. Once the SP state is found, the activation energy for the transition is given by $\Delta E^{A \to B} = E^{SP} - E^A$. For all GNEB calculations we choose a system size of 70×70 atoms with periodic boundary conditions. Here a smaller system size than for spin dynamic simulations is sufficient, because the simulation box contains only a single isolated skyrmion instead of a skyrmion lattice or spin spiral state. The preexponential factor is given by the dynamical factor v and the ratio of partition functions Z^X for the transition state ($X = $ SP) and the initial state ($X = $ A) as follows:

$$\Gamma_0^{A \to B} = \frac{v}{\sqrt{2\pi\beta}} \frac{Z^{SP}}{Z^A} = \frac{v}{\sqrt{2\pi\beta}} \frac{\prod_{n=2}^{2N} Z_n^{SP}}{\prod_{n=1}^{2N} Z_n^A}. \qquad (3)$$

Here, Z_n^X is a partition function associated with the nth eigenmode of the system

$$Z_n^X = \begin{cases} \sqrt{\dfrac{2\pi}{\beta \Omega_n^X}}, & \Omega_n^X > 0, \\ L_n^X, & \Omega_n^X = 0, \end{cases} \qquad (4)$$

where Ω_n^X denotes the nth eigenvalue of the Hessian matrix and L_n^X is the length of a mode in space of spin configurations along which the energy of the system does not change, the

zero mode. For a correct treatment of annihilation and nucleation processes it is particularly important to distinguish between harmonic modes with $\Omega_n > 0$, which describe vibrations, and zero modes with $\Omega_n \approx 0$. In this study only the skyrmion state has two zero modes corresponding to the in-plane translations and with combined length L_{1+2}^{Sk} [12,14]. Because of the different numbers of zero modes for the skyrmion, SP and FM states, the preexponential factors expressions for nucleation $\Gamma_0^{FM \to Sk}$ and annihilation $\Gamma_0^{Sk \to FM}$ of a skyrmion differ:

$$\Gamma_0^{Sk \to FM} = \frac{v L_{1+2}^{Sk}}{\beta} \frac{\prod_{n=3}^{2N} \sqrt{\Omega_n^{Sk}}}{\prod_{n=2}^{2N} \sqrt{\Omega_n^{SP}}}, \qquad (5)$$

$$\Gamma_0^{FM \to Sk} = \frac{v}{2\pi} \frac{\prod_{n=1}^{2N} \sqrt{\Omega_n^{FM}}}{\prod_{n=2}^{2N} \sqrt{\Omega_n^{SP}}}. \qquad (6)$$

III. RESULTS

In the first part of this section, we present our systematic study of how variations of the magnetic interactions affect the properties of magnetic skyrmions and their stability in Pd/Fe/Ir(111). We start with the energy dispersion of spin spirals and the magnetic phase diagram before moving to the energy barriers for skyrmion nucleation and annihilation. The transition rates are evaluated upon calculating also the preexponential factor of the Arrhenius law. In the last two sections we study the electric-field-assisted thermally activated writing and deleting of magnetic skyrmions based on solving the master equation, which allows us to directly compare our simulations to the experimental data for Pd/Fe/Ir(111) [4].

A. Spin spiral energy dispersion

In order to understand the effect of varied magnetic interactions on noncollinear spin structures, we start by analyzing the properties of homogeneous cycloidal spin spirals in our films. A cycloidal spin spiral is characterized by the wave vector $\mathbf{q}$ along which it propagates and the magnetic moment of an atom at lattice site i is given by $\mathbf{m}_i = M(\mathbf{e}_z \cos(\mathbf{q} \cdot \mathbf{R}_i) - \mathbf{e}_q \sin(\mathbf{q} \cdot \mathbf{R}_i))$, where $\mathbf{e}_z$ is the unit vector normal to the film, and $\mathbf{e}_q = \mathbf{q}/q$ is the unit vector along $\mathbf{q}$. The energy dispersion of such a spin spiral can be obtained analytically using the atomistic spin model given by Eq. (1).

In Fig. 2(a) the energy dispersion is shown for spin spirals along the high symmetry direction $\overline{\Gamma K}$ of the two-dimensional Brillouin zone (BZ), which has been obtained with the DFT-calculated values of the magnetic interactions for fcc-Pd/Fe/Ir(111) [41]. The inset of Fig. 2(a) shows that there is an energy minimum E_{min} for a spin spiral with a wave vector of $q_{min} \approx 0.06 \times 2\pi/a$, where a is the in-plane lattice constant. Note that the spin spiral dispersion is shifted with respect to the FM state (at the $\overline{\Gamma}$ point, i.e., $q = 0$) by half of the MAE $K/2$ as this term favors collinear states.

If one increases the magnitude of the nearest-neighbor exchange constant J_1 by $\delta J_1 = +0.1$ spin spirals become less favorable with respect to the FM state and therefore the energy minimum becomes more shallow and shifts to lower values of q. The opposite is true if the strength of J_1 is reduced. In a similar way, we have varied the strength of the nearest-neighbor DM interaction constant D_1 [Fig. 2(b)]. Since the DMI favors noncollinear spin states, an enhanced value of D_1 leads to a
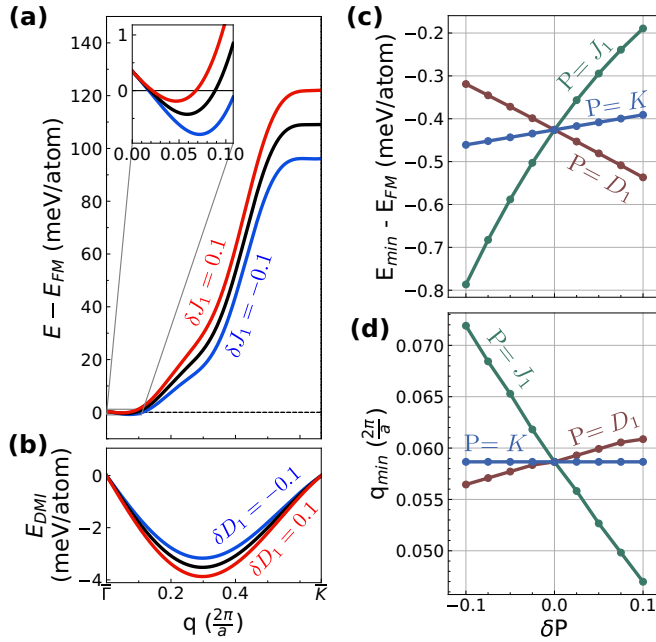
FIG. 2. (a) Energy dispersion $E(q)$ along the $\overline{\Gamma K}$ direction of the BZ for homogeneous cycloidal spin spirals in fcc-Pd/Fe/Ir(111) using the DFT-calculated parameters (black curve) and for a value of J_1 increased by 10% (red curve) and decreased by 10% (blue curve). The inset shows a zoom in the vicinity of the minima of the curves. (b) DMI contribution to the spin spirals energy for $\delta D_1 = \pm 0.1$. (c) Energy of the spin spiral minimum as a function of the interactions varied separately by δP, where $P = J_1, D_1, K$. (d) Spin spiral wave vector $q_{\min}$ of the energy minimum as a function of the variation δP.
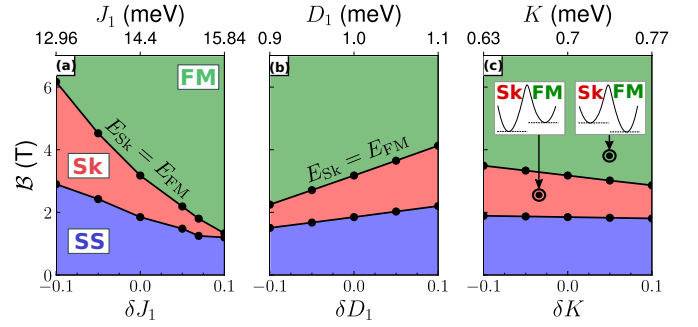

FIG. 3. Zero-temperature phase diagrams for fcc-Pd/Fe/Ir(111) as a function of magnetic field and for a variation of (a) the nearest-neighbor exchange constant J_1, (b) the DMI constant D_1, and (c) the MAE constant K. The energetically lowest phase, i.e., the FM state, the skyrmion lattice (Sk), or the spin spiral (SS) state is indicated in each plot in green, red, and blue, respectively. The black points denote the magnetic field and parameter values at which the energy of two phases is identical. The points, which indicate the calculations, have been connected by lines to show the phase boundaries.

deeper energy minimum and vice versa for a reduced DMI. Note that the effect of a variation of $\pm \delta D_1$ points qualitatively in the same direction as a variation of $\mp \delta J_1$.

We can quantify the effects by finding the energy and the wave vector of the spin spiral minimum given by $E_{\min}$ and $q_{\min}$ as a function of the variation of the interaction strengths [Figs. 2(c) and 2(d)]. In accordance with the discussion of the energy dispersion, the depth of the minimum decreases with rising exchange interaction and increases with the DMI. Since the MAE simply shifts the FM state with respect to the spin spiral energy dispersion, there is a linear decrease of $E_{\min}$ with δK [Fig. 2(c)] while the position of the spin spiral minimum, i.e., $q_{\min}$, remains unchanged [Fig. 2(d)]. It is apparent that the largest effect is obtained by a variation of the exchange interaction as it is much stronger than the other interactions in this system.

B. Zero-temperature phase diagrams

Next we discuss the zero-temperature phase diagrams of our system as a function of an external magnetic field $\mathcal{B}$ applied perpendicular to the film. Similar to Ref. [41], we compare the total energies of the FM state, the spin spiral state, and the skyrmion lattice state. We proceed as follows: For every variation δP of one of the magnetic interactions, we generate a cycloidal spin spiral with a wave vector $q_{\min}$ of the minimum of the energy dispersion [Fig. 2(d)]. For the

same parameters, we determine the skyrmion lattices with the energetically most favourable density and subsequently relax the spin spiral and skyrmion lattice states over a range of magnetic field strengths. Depending on the magnetic field strength, either the spin spiral state, the skyrmion lattice state, or the FM state is lowest in energy. The intersections of the corresponding energy curves are used to construct the parameter and magnetic field dependent zero-temperature phase diagrams, shown in Fig. 3.

At zero magnetic field, the spin spiral state is energetically lowest independent of the variation of all magnetic interactions within the given range consistent with the energy dispersion [cf. Fig. 2(a)]. At a critical magnetic field, the skyrmion lattice and spin spiral state are degenerate, which marks the onset of the skyrmion phase (Fig. 3). At an even larger magnetic field value, there is a crossover to the FM phase. The boundary between the skyrmion and FM phase is of particular interest in terms of skyrmion writing and deleting as it indicates the minimum magnetic field strength needed to obtain metastable skyrmions in the FM background.

The magnetic fields at which the transition between the phases occur depend significantly on the variation of the magnetic interactions (Fig. 3). It is clear that the largest effect occurs due to a change of the exchange constant. Since spin spirals become less favorable upon increasing J_1 [cf. Fig. 2(a)], the spin spiral and the skyrmion lattice phase shrink in size [Fig. 3(a)]. The opposite effect occurs upon increasing the DMI [Fig. 3(b)], which promotes noncollinear spin structures. Variations in the magnetocrystalline anisotropy constant [Fig. 3(c)], on the other hand, show the same trend as the exchange interaction, which is consistent with the fact that both interactions favor a collinear alignment of spins.

The boundary between the skyrmion lattice and the FM phase changes approximately linear with the magnetic interaction parameters J_1, D_1, K. We can quantify the corresponding critical magnetic field by the slope $\delta \mathcal{B}_c / \delta P$. For the nearest-neighbor exchange, the slope amounts to $-1.7\,\text{T/meV}$ or a change of $-2.4\,\text{T}$ for $\delta J_1 = 0.1$. For the

DMI, the critical magnetic field varies by 0.9 T for $\delta D_1 = 0.1$, and for the MAE, we find about 0.45 T for $\delta K = 0.1$. Relating this to real systems and assuming that our linear model for the influence of the electric field describes their behavior well enough, we can predict that opposite orientations of the field will shift the phase boundaries in opposite directions. In the next section, we will show that the rates of transitions between states exhibit the same dependence on the electric field allowing electric-field-assisted nucleation and annihilation of skyrmions.

C. Interaction dependent transition rates

Now we consider isolated skyrmions, which are metastable in the FM background for magnetic fields above the critical field $\mathcal{B}_C$, defined by

$$\mathcal{B}_C = \mathcal{B}|_{E_{Sk}=E_{FM}}. \quad (7)$$

In order to calculate the annihilation and nucleation rates of individual skyrmions we use the framework of GNEB and HTST as described in Sec. II. We compute the preexponential factors $\Gamma_0^{Sk \to FM}$ and $\Gamma_0^{FM \to Sk}$ and the corresponding activation energies $\Delta E^{Sk \to FM}$ and $\Delta E^{FM \to Sk}$ for skyrmion annihilation $Sk \to [SP]^{\ddagger} \to FM$ and skyrmion nucleation $FM \to [SP]^{\ddagger} \to Sk$, respectively. With these two quantities we can calculate the rates and lifetimes based on the Arrhenius law, i.e., Eq. (2).

As in the previous section, we vary the magnetic interactions by $\pm 10\%$. For each of these sets of parameters an isolated skyrmion is minimised with respect to energy using damped spin dynamics simulation. Afterwards, the MEP for a transition from the skyrmion state to the FM state is calculated. From the MEP the activation energies, defined as the energy difference between the FM or Sk state and the saddle point, can be extracted as illustrated in Fig. 4 for a magnetic field of $\mathcal{B} = 4$ T.

The energy barrier can be decomposed into the contributions from the interactions, which enter our spin model [cf. Eq. (1)]. Since the DMI favors the skyrmion state, it provides a large part of the energy barrier [Fig. 4(a)]. The MAE and the Zeeman energy prefer the FM state and lower the total barrier. Due to the strong exchange frustration, which is present in Pd/Fe/Ir(111) [41,46], the exchange term contributes significantly to the barrier and to the stability of the skyrmion state against a collapse into the FM state. The saddle point structure [Fig. 4(b)] is characteristic for the radial collapse mechanism (see e.g. Refs. [25,41]) in which the skyrmion shrinks along the MEP until at the saddle point the inner spins point almost in-plane towards each other.

We have performed GNEB calculations such as that presented in Fig. 4 at magnetic fields above the critical field $\mathcal{B}_C$ for varied strength of the exchange interaction, the DMI, and the MAE. From these calculations we obtain the skyrmion radius R_{Sk}, and the activation energies $\Delta E^{Sk \to FM}$ and $\Delta E^{FM \to Sk}$. From the saddle points of the MEP, the preexponential factors for the transitions can be calculated using Eq. (5). The results are shown in Fig. 5. The data is presented for a certain range of magnetic fields relative to the critical magnetic field $\mathcal{B}_C$ at which Sk and FM states are degenerate (the border between the Sk and the FM phases shown in
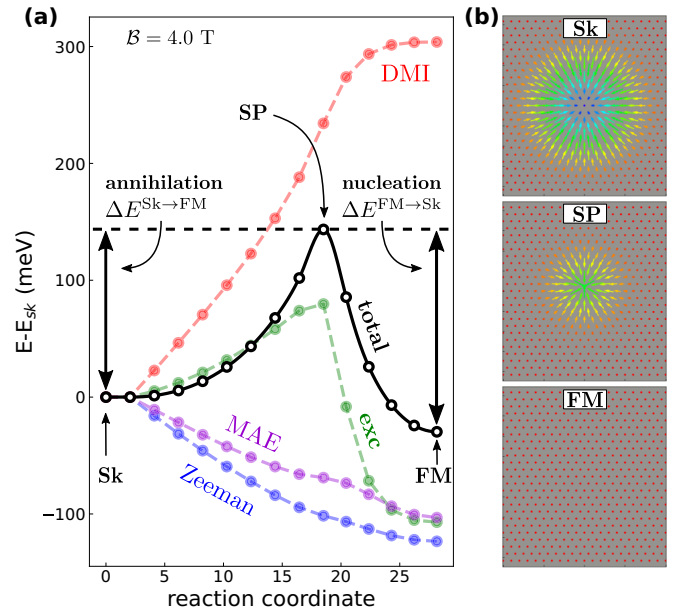

FIG. 4. (a) Minimum energy path for a transition between the skyrmion (Sk) and the FM state at $\mathcal{B} = 4.0$ T. The total energy (black) along the path is displayed as well as the contributions from the DMI (red), the exchange interaction (green), the MAE (purple), and the Zeemann interaction (blue). The saddle point of the transition is marked and the activation energies for skyrmion nucleation $\Delta E^{FM \to Sk}$, and skyrmion annihilation $\Delta E^{Sk \to FM}$, are indicated. (b) Spin structures of the Sk state, the FM state, and the saddle point on the minimum energy path. The skyrmion collapse occurs via radially-symmetrical shrinking.

Fig. 3). Note that $\mathcal{B}_C$ also marks the point at which activation energies for skyrmion nucleation and annihilation are equal.

We notice that a variation of the interaction constants by $\pm 10\%$ leads—especially for the exchange interaction—to significant changes of skyrmion properties. Lowering the nearest-neighbor exchange constant leads to smaller skyrmions, enhancing it will let them grow in size [Fig. 5(a)]. The radius is hereby estimated by fitting a radial symmetric skyrmion profile [6,24] to the states relaxed by spin dynamics. Since lowering the first-neighbor exchange interaction makes noncollinear structures less costly, smaller skyrmions with bigger angles between adjacent spins can be realised. Consequently the DMI has exactly the opposite effect on the skyrmion size [Fig. 5(b)]. The influence of varying the anisotropy on the skyrmion radius can be neglected [Fig. 5(c)].

The energy barriers for skyrmion nucleation and annihilation are strongly affected upon variation of the exchange constant [Fig. 5(d)], e.g., at the critical magnetic field there is a shift by about 100 meV between the case of decreasing and increasing J_1 by 10%. A correlation with the skyrmion radius is observed, i.e., larger skyrmions show higher activation energies with respect to a transition to the FM state. This is in good agreement with previous reports on the relation of skyrmion size and stability [23,24]. A variation of the DMI or the MAE has a much smaller effect on the energy barriers: The corresponding changes in the energy barrier are barely visible in Figs. 5(e) and 5(f).
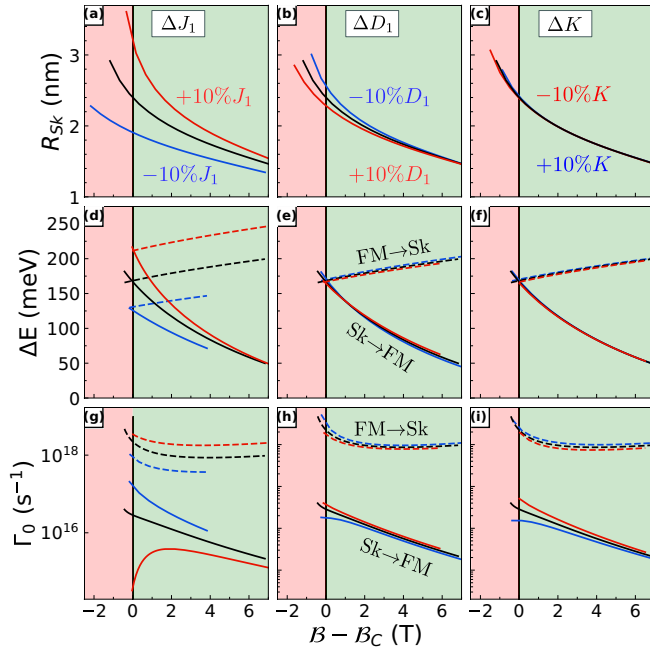
FIG. 5. Variation of the properties of isolated skyrmions in fcc-Pd/Fe/Ir(111) upon changing the magnetic interactions. [(a)–(c)] skyrmion radius, [(d)–(f)] collapse and creation barrier, and [(g)–(i)] preexponential factors as functions of the external magnetic field upon varying the nearest-neighbor exchange constant J_1, the nearest-neighbor DMI D_1, or the magnetocrystalline anisotropy energy K, respectively. The constants are varied by $\pm 10\%$. All quantities are plotted relative to the critical magnetic field $\mathcal{B}_C$. The background color indicates the energetically lowest phase: skyrmion lattice (red) or the FM state (green).

For the preexponential factors we find that variations in the first neighbor exchange interaction have a large effect on the shape of the curves, especially close to $\mathcal{B}_C$ [Fig. 5(g)]. A rising exchange interaction leads to a higher preexponential factor for nucleation and makes it therefore more likely for a skyrmion state to be created. The preexponential factor for annihilation, on the other hand, drops, which makes it also less likely for the skyrmion state to be destroyed. This rapid dropping of the preexponential factor for $\mathcal{B} \to \mathcal{B}_C$ has been found before for hcp-Pd/Fe/Ir(111) [26]. Taken together, the influence of rising nearest-neighbor exchange interaction on the preexponential factor makes it more likely to find a skyrmion state present in the system. Upon decreasing the exchange constant we observe the opposite trend. The nucleation becomes less favorable and the probability for annihilation rises, overall shifting the stability towards the FM state. Therefore, our results suggest that larger skyrmions in fcc-Pd/Fe/Ir(111), found for rising exchange constant J_1, are stabilised by both enhanced energy barrier and small preexponential factor. The preexponential factor is much less but still noticeably affected upon a variation of the DMI or the MAE, in particular, for the skyrmion collapse [Figs. 5(h) and 5(i)].

D. Ratio of transition rates

With the preexponential factors and the activation energies, we can compute the transition rates according to Eq. (2) and
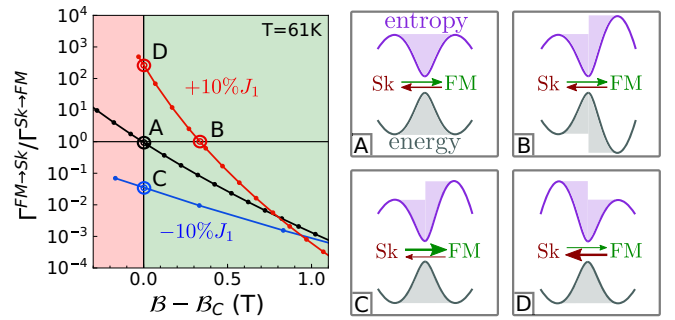

FIG. 6. Calculated ratio of transition rates for J_1 varied by $\pm 10\%$. Temperature is chosen to be $T = 61$ K, since nucleation and annihilation rates for the undisturbed system are equal at $\mathcal{B} = \mathcal{B}_C$ for this temperature, illustrated by point A. Points B, C, and D illustrate the accomplishment of the ratio of transition rates for other combinations of J_1 and $\mathcal{B}$. The energy difference of states is thereby sketched by the grey line and the temperature dependent contribution from entropy [Eq.(8)] is sketched in purple.

subsequently the ratio $\Gamma^{\mathrm{FM}\to\mathrm{Sk}}/\Gamma^{\mathrm{Sk}\to\mathrm{FM}}$. This ratio indicates whether the nucleation or the annihilation of a skyrmion is more likely to happen for a given set of magnetic interactions. In Fig. 6 these ratios are shown for the example of varied nearest-neighbor exchange interaction. The results are displayed with respect to the critical magnetic field $\mathcal{B}_C$, so that $\mathcal{B} - \mathcal{B}_C = 0$ marks the point at which the activation energies for nucleation and annihilation are equal. Nevertheless, the ratios of transition rates for different exchange interactions differ by many orders of magnitude at this point. Consequently, this has to be due to the preexponential factor [cf. Fig. 5(g)]. Since the preexponential factor is linked to the entropy difference of states ΔS [26,51], this behavior demonstrates that the free energy ΔF must be taken into account as the thermodynamic potential for annihilation and nucleation processes.

To show this explicitly, we compute the free energy $F_A = -k_B T \ln Z_A$ of a state A in harmonic approximation as shown in Appendix B. We find that the difference in free energy between the transition state SP and the initial state A, the partition functions of which are treated according to Ref. [52], can be written as

$$\Delta F^{\mathrm{A}\to\mathrm{B}} = \Delta U^{\mathrm{A}\to\mathrm{B}} - T\Delta S^{\mathrm{A}\to\mathrm{B}} \tag{8}$$

$$= \Delta E^{\mathrm{A}\to\mathrm{B}} - k_B T \ln\left(\frac{\prod_{n=2}^{2N} Z_n^{\mathrm{SP}}}{\prod_{n=1}^{2N} Z_n^{\mathrm{A}}}\right) \tag{9}$$

with $\Delta U^{\mathrm{A}\to\mathrm{B}}$ being the difference in internal energy (cf. Appendix B) and $\Delta E^{\mathrm{A}\to\mathrm{B}}$ the energy barrier for the process. Comparing this expression with Eq. (2) we can write the transition rates as

$$\Gamma^{\mathrm{A}\to\mathrm{B}} = \frac{v}{\sqrt{2\pi\beta}}\exp(-\beta\Delta F^{\mathrm{A}\to\mathrm{B}}). \tag{10}$$

In this form, the ratio of transition rates becomes easy to handle, because the dynamical factor depends only on the saddle
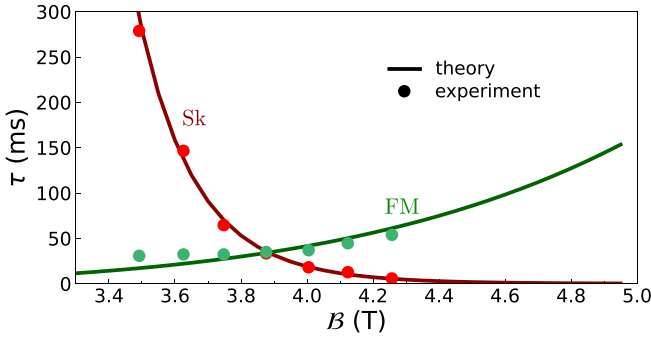
FIG. 7. Comparison of experimental data for the lifetimes of the FM state and skyrmions in Pd/Fe/Ir(111) [20] (green and red filled circles, respectively) and those obtained via atomistic spin simulations (green and red lines) based on HTST with DFT-calculated parameters for all magnetic interactions. The numerically obtained lifetimes have been evaluated at an effective temperature of $T_{\text{eff}} = 54.3$ K, which simulates the effect of hot electron injection [25].

point configuration, which is the same for both nucleation and annihilation. Therefore we obtain

$$\frac{\Gamma^{\text{FM}\to\text{Sk}}}{\Gamma^{\text{Sk}\to\text{FM}}} = \exp[-\beta(\Delta F^{\text{FM}\to\text{Sk}} - \Delta F^{\text{Sk}\to\text{FM}})]$$
$$= \exp[\beta(F_{\text{FM}} - F_{\text{Sk}})], \qquad (11)$$

where all contributions from the SP cancel out. From this expression we can see that the relative frequency for nucleation and annihilation processes to happen depends only on the free energy difference of the initial and the final state. Information on the saddle point is not required, only its existence matters. This gives rise to an easy understanding of the features in Fig. 6. The situation is illustrated at the marked points. One can see that a difference in energy can be compensated through entropy (point B) and that even for equal energies, a difference in entropy can change the ratio of transition rates by more than one order of magnitude (points C, D).

E. Calculated vs experimental lifetimes

Before we address the issue of electric-field-assisted switching, we compare the lifetimes obtained for Pd/Fe/Ir(111) based on our approach with experimental data. In spin-polarised scanning tunneling microscopy (SP-STM) experiments the switching rate and thus the average lifetime of the FM state and magnetic skyrmions can be determined from telegraph noise measurements [4,20,25]. In the work of Hagemeister *et al.* [20] the lifetimes in Pd/Fe/Ir(111) have been obtained as a function of the applied magnetic field (Fig. 7). We find an excellent agreement of the experimental data and our atomistic spin simulations (Fig. 7) based on the DFT-calculated parameters for fcc-Pd/Fe/Ir(111) [41] and a single fitting parameter, the effective temperature, which describes the average sample temperature beneath the tip after hot electron injection [25].

The best fitting effective temperature for an agreement between experimental data and simulation is found for $T_{\text{eff}} = (54.29 \pm 0.02)$ K, similar to that of about 50 K reported in Ref. [25] to match the experimental data [53].

TABLE I. Slopes for shell resolved exchange interaction parameters J_n over an applied electric field $\mathcal{E}$ perpendicular to the surface, estimated by DFT calculations for fcc-Pd/Fe/Ir(111) [47]. The slopes are in units of meV/(V/Å).

$\Delta J_1/\Delta\mathcal{E}$	$\Delta J_2/\Delta\mathcal{E}$	$\Delta J_3/\Delta\mathcal{E}$	$\Delta J_4/\Delta\mathcal{E}$	$\Delta J_5/\Delta\mathcal{E}$
0.58	0.0	−0.01	−0.02	0.05

Regarding the lifetime of the FM state we assume that the skyrmion can nucleate at any point below the STM tip with equal probability. The HTST method used for the calculation of transition rates returns the rate per saddle point. Therefore, the transition rate for skyrmion creation $\Gamma^{\text{FM}\to\text{Sk}}$ has to be scaled with the number of possible saddle points σ and the lifetime of the FM state consequently by σ^{-1}. A two-dimensional lattice consisting of $N \times N$ atoms has $N_{\text{uc}} = (N-1)^2$ unit cells and two possible saddle points per unit cell, which leads to a factor for the mean FM lifetime of $\sigma = 2N_{\text{uc}} = 2(N-1)^2$. We have used the value of σ as a fitting parameter in order to match the experimental data for the lifetime of the FM state. The effective temperature has been fixed to the value obtained from the fit of the skyrmion lifetime, i.e., $T_{\text{eff}} = 54.3$ K.

A value of $\sigma^{-1} = 4.5 \times 10^{-3}$, which corresponds to $N \approx 12$, yields good agreement between the simulation and the experiment (cf. green curve in Fig. 7). So by assuming that all unit cells underneath the STM tip have the same probability to be the central location of the saddle point and that all transitions are activated thermally, the scaling factor σ indicates that transitions in an area of 12×12 atoms are responsible for the measured lifetime. Considering the lattice constant $a_{\text{Ir}} = 0.275$ nm of Ir, this results in a nucleation area of about $A_{\text{nuc}} = (Na_{\text{Ir}})^2 \sin\frac{\pi}{3} \approx 9.43$ nm^2 on the hexagonal lattice. This area is on the same order of magnitude as that of the skyrmion based on the radius of about 2.3 nm (Fig. 5) for the given range of magnetic fields. Nevertheless the STM-tip's real electric field is inhomogenous and this estimation of the nucleation area must be understood as an approximation. Note that a similar scaling factor for the skyrmion creation transition rates has been used in Ref. [25], which was based on experimentally determined nucleation area and led to good agreement between theory and experiment. We conclude that our atomistic spin simulations based on a spin model fully parametrized from DFT calculations provide quantitatively good description of the creation and collapse rates of skyrmions in Pd/Fe/Ir(111).

F. Electric-field-assisted switching

Finally, we model the effect of the electric field on the switching rates of the FM and skyrmion state in Pd/Fe/Ir(111). For this purpose, we use DFT-calculated values of the exchange constants obtained for electric fields of $\mathcal{E} = \pm 0.5$ V/Å [47]. For fcc-Pd/Fe/Ir(111) the values are given in Table I. We modify only the exchange constants here since it was found within the DFT calculations that the DMI and the MAE are influenced much less. This can be understood based on the spin-dependent screening of the

electric field at the surface layers of Pd/Fe/Ir(111). Since the screening charge is only significant in the first and second atomic layer (compare e.g., Ref. [40]), only the Pd/Fe interface is much affected. The hybridization at this interface has a strong effect on the exchange constants in the Fe layer [46,54]; however, it provides only a small contribution to the interactions of relativistic origin such as the DMI and MAE since Pd is a 4*d* transition metal. In contrast, the Fe/Ir interface is already effectively screened from the electric field and thus provides only a minor contribution to the changes of the magnetic interactions. The variation of the different magnetic interactions due to the applied electric field can be explained based on the spin-dependent screening charge in the film as discussed in detail in Refs. [36,40]. Note that electric field effects on the exchange interaction, which are even by a factor of about two larger than in Pd/Fe/Ir(111) have been reported based on DFT studies for film systems with a Co [36] or an Fe [40] monolayer directly at the surface. The induced change in the exchange constant J_1 amounts to $\Delta J_1 = \pm 0.29$ meV for an electric field of $\mathcal{E} = \pm 0.5$ V/Å (cf. Table I). This corresponds to a relative variation of only $\sim 2\%$.

First, we have obtained the zero-temperature magnetic phase diagram as a function of the electric field [Fig. 8(a)] using the field-dependent variation of the exchange interactions $\Delta J_i / \Delta \mathcal{E}$, from DFT (Table I) and assuming a linear field dependence. The phase boundary between the skyrmion and FM phase is given by the condition of equal skyrmion nucleation and annihilation rates, which includes the attempt frequencies as discussed in Sec. III D and the scaling factor σ. The transition rates have been evaluated at an effective temperature of $T_{\text{eff}} = 54.3$ K as in the previous section to simulate the effect of hot electron injection in an STM [25]. For comparison, the dashed line in Fig. 8(a) indicates the locus of equal energies of the skyrmion lattice and FM phase obtained as in Fig. 3. The difference in position and slope of these two lines arises from preexponential factor and its dependence on the exchange interactions (Fig. 5). The slope $\partial \mathcal{B}_{\text{C}} / \partial \mathcal{E}$ of the change of the critical magnetic field $\mathcal{B}_{\text{C}}$ with the electric field amounts to -1.06 T/(V/Å). This value is quite significant in agreement with our systematic study (Fig. 3).

The transition rates are calculated at $T_{\text{eff}} = 54.3$ K for electric fields $\mathcal{E} = \pm 0.5$ V/Å with modified exchange interactions according to Table I. In order to show that an electric field can be used to write or delete individual skyrmions, we go beyond discussing how the ratio of transition rates changes and to quantify the switching probability. We therefore compute the probability P_∞^{Sk} for finding a skyrmion at a time $t \to \infty$. This quantity can be calculated based on the master equations [55] and the transition rates for the two-state system given by the skyrmion and the FM state:

$$\frac{dp_{\text{A}}(t;x)}{dt} = -p_{\text{A}}(t;x)\Gamma^{\text{A}\to\text{B}} + p_{\text{B}}(t;x)\Gamma^{\text{B}\to\text{A}} \quad (12)$$

$$\frac{dp_{\text{B}}(t;x)}{dt} = -p_{\text{B}}(t;x)\Gamma^{\text{B}\to\text{A}} + p_{\text{A}}(t;x)\Gamma^{\text{A}\to\text{B}} \quad (13)$$

where $p_y(t;x)$ is the time dependent probability to find the system in state $y = \text{A, B}$ after has been initialised in the state $x = \text{A, B}$ at $t = 0$. As shown in Ref. [55] this system of
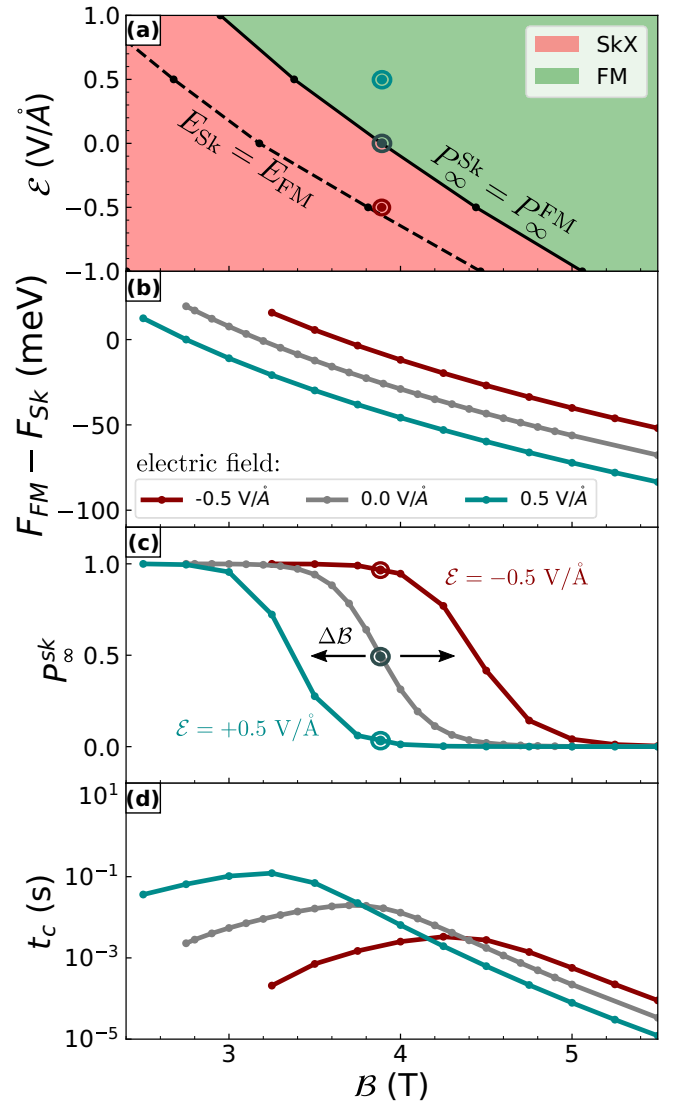

FIG. 8. (a) Phase diagram at $T_{\text{eff}} = 54.3$ K for the electric and magnetic field dependence of skyrmion (red), spin spiral (blue), and FM (green) phases in Pd/Fe/Ir(111). The dashed line indicates where the energies of FM and Sk state are equal. The solid line indicates where the temperature dependent static distributions are equal. (b) The free energy differences of Sk and FM states shown for zero electric field (grey) and $\mathcal{E} = \pm 0.5$ V/Å. (c) Static distributions for the same electric fields. (d) Characteristic time for thermally activated transitions between Sk and FM state.

equations can be solved analytically

$$p_{\text{A}}(t;x) = p_{\text{A}}(0;x) \frac{\Gamma^{\text{B}\to\text{A}} + \Gamma^{\text{A}\to\text{B}} e^{-\omega t}}{\omega}$$

$$+ p_{\text{B}}(0;x) \frac{\Gamma^{\text{B}\to\text{A}}(1 - e^{-\omega t})}{\omega} \quad (14)$$

with $\omega = \Gamma^{\text{A}\to\text{B}} + \Gamma^{\text{B}\to\text{A}} = t_c^{-1}$ being the inverse of the characteristic time t_c. The stationary distribution is then defined as the probability to find the system in either state A or B once it reached thermal equilibrium after initialization. Note that this quantity is independent of the initial state x, chosen, e.g., by

setting $p_y(t_0; x) = 1$ if $x = y$ and zero otherwise

$$P_\infty^A = \lim_{t \to \infty} p_A(t; A) = \lim_{t \to \infty} p_A(t; B) = \frac{\Gamma^{B \to A}}{\omega} \qquad (15)$$

and respectively $P_\infty^B = 1 - P_\infty^A$. Therefore, the stationary distribution can be directly computed from the transition rates.

Taking the scaling of the nucleation rates by the factor σ from Sec. III E into account and using the relation to the free energy from Eq. (11), the stationary distribution for skyrmions in harmonic approximation to the energy takes the form of an Fermi-Dirac distribution with respect to the free energy difference of skyrmion and FM state

$$P_\infty^{Sk} = \frac{\sigma \Gamma^{FM \to Sk}}{\sigma \Gamma^{FM \to Sk} + \Gamma^{Sk \to FM}} \qquad (16)$$

$$= \frac{1}{1 + e^{-\beta(F_{FM} - F_{Sk}) - \ln \sigma}}. \qquad (17)$$

Here the scaling factor σ acts as a shift for the distribution. Note that P_∞^{Sk} does not depend on information on the saddle point itself.

The free energy difference of the skyrmion and the FM state can be computed from the transition rates by rearranging Eq. (11) and the result is shown in Fig. 8(b). It can be observed that the free energy difference of states is not a perfect linear function with respect to the external magnetic field, but rather a polynomial of higher degree. Because of this, the form of the probability functions shown in Fig. 8(c) are not perfect Fermi-Dirac distributions with respect to the magnetic field.

We want to evaluate the probabilities for a fixed magnetic field, in order to quantify the influence of electric fields on the probability to write or delete a skyrmion in Pd/Fe/Ir(111). We choose $\mathcal{B} = 3.89$ T as working point, because at zero electric field the probability for finding a skyrmion is then given by $P_\infty^{Sk} = P_\infty^{FM} = 0.5$. In fact, we observe in Fig. 8(c) that applying an electric field with negative sign of $\mathcal{E} = -0.5$ V/Å leads to a probability of ∼96% for finding a skyrmion, while applying an electric field of $\mathcal{E} = +0.5$ V/Å leads to a probability of also ∼96% for finding the FM state present. This behavior is illustrated by the marked points in Fig. 8(c). Therefore, our calculations demonstrate that for Pd/Fe/Ir(111) an electric-field-assisted nucleation and annihilation of skyrmions is possible, if the magnetic field is chosen in the vicinity of the critical magnetic field as in the STM experiments of Romming *et al.* [4]. This switching comes along with a transition between the phases, as indicated by the phase diagram in Fig. 8(a).

The qualitative agreement between the calculated skyrmion probability function at electric fields of $\mathcal{E} = \pm 0.5$ V/Å [Fig. 8(c)] and the experimentally obtained probability curves at bias voltages of $U = \pm 0.6$ V (Fig. 4 c of Ref. [4]) is remarkable. Note that the sign of the shift agrees between experiment and simulation since a negative bias voltage in the experiment corresponds to a positive electric field and vice versa [4,33] (cf. Fig. 1).

In the experimental data the magnetic field shift between the two probability curves at opposite bias voltages amounts to about $\Delta B \approx 0.1$ T. In our simulations, the shift between the curves at the opposite electric field values is about 1 T,

i.e., by a factor of 10 or larger. Therefore, already a smaller electric field of only $\mathcal{E} = 0.05$ V/Å would be sufficient to explain the magnitude of the experimental effect. This is a reasonable value at the given experimental bias voltage of $U = 0.6$ V since the tip-surface distance is $d \approx 5$ to 10 Å, i.e., $\mathcal{E} \approx -U/d = 0.06$ to 0.12 V/Å. Therefore, the agreement of our simulations based on DFT-calculated parameters is even quantitatively very good.

The characteristic time t_c can be computed from transition rates. It indicates how long it takes the system to reach thermal equilibrium after being initialised in one of the two possible states. Therefore it can be interpreted as the average switching time for nucleation and annihilation processes, if one considers only thermally activated transitions. In Fig. 8(d) it can be observed that the characteristic time varies over two to three orders of magnitude in the interesting range of magnetic fields. For each electric field the switching time is maximal, when the stationary distribution holds $P_\infty^{Sk} = P_\infty^{FM} = 0.5$. Since at this point none of the states is favoured over the other, this finding is in good agreement with physical intuition. We also observe that applying a positive electric field at $\mathcal{B} = 3.89$ T leads to no significant changes in the switching time, while applying a negative field reduces it. Therefore we can conclude that electric-field-assisted nucleation and annihilation processes can occur on different time scales.

In other ultrathin film systems the DMI and the MAE may also contribute to the electric-field-assisted switching as investigated in terms of the transition rates in the first part of Sec. III. The interplay of the electric-field-induced changes of exchange, DMI, and MAE may then—depending on the electronic structure of the system—either increase or decrease the total effect on the transition rates. However, the solution of the master equations and the form of the probability function presented in this section will not be affected since it depends only on the difference between the free energies of the skyrmion and FM state.

IV. CONCLUSIONS

We investigated electric-field-assisted thermally activated nucleation and annihilation of magnetic skyrmions in the ultrathin film system Pd/Fe/Ir(111) based on an atomistic spin model with all magnetic interaction constants obtained from DFT. The transition rates were calculated by the combination of atomistic spin dynamics simulations, the geodesic nudged elastic band method and harmonic transition state theory. The calculated magnetic-field-dependent skyrmion lifetimes for Pd/Fe/Ir(111) are in good agreement with experimental STM data of Ref. [20].

Our study shows that the electric-field-induced change of the exchange interaction may play a more crucial role for switching than assumed in previous studies, which only considered the effect of the DMI. The field-induced variation of the magnetic interactions shifts the critical magnetic fields between the spin spiral, the skyrmion lattice, and the field-polarized (ferromagnetic) phase. They also have significant influence on the activation energies and the preexponential factors for creation and collapse of skyrmions. The ratio of skyrmion nucleation and annihilation rates, which is crucial for thermally activated switching assisted by an electric field

TABLE II. List of magnetic interaction constants for fcc-Pd/Fe/Ir(111) determined from DFT as given in Ref. [41].

Shell n	J_n (meV)	D_n (meV)
1	14.4046	1.0
2	−2.48108	
3	−2.68507	
4	0.520605	
5	0.73757	
6	0.277615	
7	0.160881	
8	−0.57445	
9	−0.212654	

is shown to be directly related to the free energy difference between the skyrmion and the FM state. Depending on the sign of the electric field, the ratio favors either the skyrmion or the FM state, which supports field assisted switching.

We simulated the electric-field-assisted switching by calculating the skyrmion probability as a function of the magnetic field based on the master equations. We used the transition rates obtained numerically with the DFT-calculated parameters of the magnetic interactions for Pd/Fe/Ir(111) at electric fields of $\mathcal{E} = \pm 0.5$ V/Å. The probability function can be related to the free energies of the skyrmion and the FM state and it resembles a Fermi-Dirac distribution.

The effect of the electrical field on writing and deleting of skyrmions obtained from our simulations for Pd/Fe/Ir(111) is significant and can explain the experimental observations in Ref. [4]. Note that these STM experiments were performed using magnetic tips and the writing and deleting of magnetic skyrmions was attributed to the spin-transfer torque effect. In order to distinguish between both effects experimentally nonmagnetic tips are required as in the experiments reported in Ref. [33]. Our study suggests that electric fields play a more significant role for skyrmion writing and deleting in STM experiments than anticipated previously [4] and that the electric-field-induced change of the exchange interaction can be essential.

ACKNOWLEDGMENTS

APPENDIX A: INTERACTION PARAMETERS

The shell resolved exchange and DMI constants for fcc-Pd/Fe/Ir(111) are taken from DFT as given in Ref. [41] and listed in Table II. The magnetocrystalline anisotropy constant is $K = 0.7$ meV and favors a magnetization perpendicular to the surface. The magnetic moment for each spin has been set to $M = 3.0\mu_B$ as in Ref. [41].

APPENDIX B: TRANSITION RATE VIA FREE ENERGY DIFFERENCE

Consider a system of N magnetic moments coupled to a heat bath of temperature T and that is in a state A. The partition function Z^A of that state is defined by

$$Z^A = Y \int_{-\infty}^{\infty} e^{-\beta E^A} dE^A \qquad (B1)$$

$$= Y \int_{-\infty}^{\infty} \exp\left(-\beta\left[E_0^A + \sum_{n=1}^{2N} \frac{\Omega_n}{2} q_n^2\right]\right) dq_1 \dots \qquad (B2)$$

$$= Y e^{-\beta E_0^A} \prod_{n=1}^{2N} \underbrace{\int_{-\infty}^{\infty} \exp\left(-\frac{\beta\Omega_n}{2} q_n^2\right) dq_n}_{=:Z_n^A} \qquad (B3)$$

$$= Y e^{-\beta E_0^A} \prod_{n=1}^{2N} Z_n^A \qquad (B4)$$

with normalisation constant Y. Here we used that due to the harmonic approximation to the energy $E = E_0 + \frac{1}{2}\sum \Omega_n q_n^2$ we can separate the integrals, where Ω_n are the Hessian eigenvalues and q_n the normal coordinates of the nth mode.

For the transition state however the situation is different. The dividing surface for a reaction is defined as the $(2N-1)$-dimensional hyperplane perpendicular to the unstable mode of the transition state SP. In order to define the partition function for this state in $2N$ coordinates, we assume a subspace of thickness ξ surrounding the dividing surface in the direction of the unstable mode. According to [52] the partition function for the transition state is given by

$$Z^{SP} = \xi Z^{\ddagger} = \xi Y e^{-\beta E_0^{SP}} \prod_{n=2}^{2N} Z_n^{\ddagger} \qquad (B5)$$

where $Z^{\ddagger}$ is the partition function of the $(2N-1)$-dimensional dividing surface. From these partition functions, we compute the difference in internal energy $\Delta U^{A \to B}$, free energy $\Delta F^{A \to B}$, and entropy $\Delta S^{A \to B}$ of initial state A and transition state SP restricted to the dividing surface

$$\Delta F^{A \to B} = -k_B T (\ln Z^{\ddagger} - \ln Z^A) \qquad (B6)$$

$$= \Delta E^{A \to B} - k_B T \ln\left(\frac{\prod_{n=2}^{2N} Z_n^{\ddagger}}{\prod_{n=1}^{2N} Z_n^A}\right) \qquad (B7)$$

$$\Delta S^{A \to B} = -\frac{\partial \Delta F^{A \to B}}{\partial T} \qquad (B8)$$

$$= k_B \ln\left(\frac{\prod_{n=2}^{2N} Z_n^{\ddagger}}{\prod_{n=1}^{2N} Z_n^A}\right) + \frac{k_B}{2} \Delta N_{>0}^{A \to B} \qquad (B9)$$

$$\Delta U^{A \to B} = -\frac{\partial}{\partial \beta}(\ln Z^{\ddagger} - \ln Z^A) \qquad (B10)$$

$$= \Delta E^{A \to B} + \frac{k_B T}{2} \Delta N_{>0}^{A \to B} \qquad (B11)$$

with energy barrier $\Delta E^{\mathrm{A}\to\mathrm{B}} = E_0^{\mathrm{SP}} - E_0^{\mathrm{A}}$ and the difference in the number of harmonic degrees of freedom $\Delta N_{>0}^{\mathrm{A}\to\mathrm{B}} = N_{>0}^{\ddagger} - N_{>0}^{\mathrm{A}}$. The expressions above fulfill

$$\Delta F^{\mathrm{A}\to\mathrm{B}} = \Delta U^{\mathrm{A}\to\mathrm{B}} - T\,\Delta S^{\mathrm{A}\to\mathrm{B}}. \tag{B12}$$

For deriving Eqs. (B7), (B9), and (B11) we considered the internal temperature dependence of the partition functions from Eq. (4)

$$\frac{\partial Z_n}{\partial T} = \begin{cases} \frac{Z_n}{2T} & \text{if} \quad \Omega_n > 0 \\ 0 & \text{if} \quad \Omega_n = 0 \end{cases} \tag{B13}$$

$$\frac{\partial Z_n}{\partial \beta} = \begin{cases} -\frac{Z_n}{2\beta} & \text{if} \quad \Omega_n > 0 \\ 0 & \text{if} \quad \Omega_n = 0 \end{cases} \tag{B14}$$

consequently leading to

$$\frac{\partial}{\partial T} \ln\left(\prod_{n=1}^{2N} Z_n\right) = \sum_{n=1}^{2N} \frac{1}{Z_n}\frac{\partial Z_n}{\partial T} = \frac{1}{2T}N_{>0} \tag{B15}$$

$$\frac{\partial}{\partial \beta} \ln\left(\prod_{n=1}^{2N} Z_n\right) = -\frac{1}{2\beta}N_{>0}. \tag{B16}$$

Here the number of nonzero derivatives is given by the number $N_{>0}$ of Hessian eigenmodes with $\Omega_n > 0$. Furthermore the expression for the transition rate in HTST [Eq. (2)] can be written in terms of free energy using Eq. (B7)

$$\Gamma^{\mathrm{A}\to\mathrm{B}} = \frac{v}{\sqrt{2\pi\beta}}\frac{\prod_{n=2}^{2N} Z_n^{\mathrm{SP}}}{\prod_{n=1}^{2N} Z_n^{\mathrm{A}}} \exp(-\beta\Delta E^{\mathrm{A}\to\mathrm{B}}) \tag{B17}$$

$$= \frac{v}{\sqrt{2\pi\beta}} \exp(-\beta\Delta F^{\mathrm{A}\to\mathrm{B}}). \tag{B18}$$

---

[1] S. Mühlbauer, B. Binz, F. Jonietz, C. Pfleiderer, A. Rosch, A. Neubauer, R. Georgii, and P. Böni, Science **323**, 915 (2009).

[2] X. Yu, Y. Onose, N. Kanazawa, J. H. Park, J. Han, Y. Matsui, N. Nagaosa, and Y. Tokura, Nature (London) **465**, 901 (2010).

[3] S. Heinze, K. Von Bergmann, M. Menzel, J. Brede, A. Kubetzka, R. Wiesendanger, G. Bihlmayer, and S. Blügel, Nat. Phys. **7**, 713 (2011).

[4] N. Romming, C. Hanneken, M. Menzel, J. E. Bickel, B. Wolter, K. von Bergmann, A. Kubetzka, and R. Wiesendanger, Science **341**, 636 (2013).

[5] A. N. Bogdanov and D. Yablonskii, Zh. Eksp. Teor. Fiz **95**, 178 (1989) [Sov. Phys. JETP **68**, 101 (1989)].

[6] A. Bocdanov and A. Hubert, Phys. Status Solidi B **186**, 527 (1994).

[7] J. Grollier, D. Querlioz, K. Camsari, K. Everschor-Sitte, S. Fukami, and M. D. Stiles, Nat. Electron. **3**, 360 (2020).

[8] D. Pinna, F. Abreu Araujo, J.-V. Kim, V. Cros, D. Querlioz, P. Bessière, J. Droulez, and J. Grollier, Phys. Rev. Applied **9**, 064018 (2018).

[9] K. M. Song, J.-S. Jeong, B. Pan, X. Zhang, J. Xia, S. Cha, T.-E. Park, K. Kim, S. Finizio, J. Raabe *et al.*, Nat. Electron. **3**, 148 (2020).

[10] A. Fert, V. Cros, and J. Sampaio, Nat. Nanotechnol. **8**, 152 (2013).

[11] R. Tomasello, E. Martinez, R. Zivieri, L. Torres, M. Carpentieri, and G. Finocchio, Sci. Rep. **4**, 6784 (2015).

[12] P. F. Bessarab, G. P. Müller, I. S. Lobanov, F. N. Rybakov, N. S. Kiselev, H. Jónsson, V. M. Uzdin, S. Blügel, L. Bergqvist, and A. Delin, Sci. Rep. **8**, 3433 (2018).

[13] X. Zhang, M. Ezawa, and Y. Zhou, Sci. Rep. **5**, 9400 (2015).

[14] S. Haldar, S. von Malottki, S. Meyer, P. F. Bessarab, and S. Heinze, Phys. Rev. B **98**, 060413(R) (2018).

[15] S. Meyer, M. Perini, S. von Malottki, A. Kubetzka, R. Wiesendanger, K. von Bergmann, and S. Heinze, Nat. Commun. **10**, 3823 (2019).

[16] N. Nagaosa and Y. Tokura, Nat. Nanotechnol. **8**, 899 (2013).

[17] A. Belavin and A. Polyakov, JETP Lett. **22**, 245 (1975).

[18] A. Abanov and V. L. Pokrovsky, Phys. Rev. B **58**, R8889 (1998).

[19] J. Sampaio, V. Cros, S. Rohart, A. Thiaville, and A. Fert, Nat. Nanotechnol. **8**, 839 (2013).

[20] J. Hagemeister, N. Romming, K. Von Bergmann, E. Vedmedenko, and R. Wiesendanger, Nat. Commun. **6**, 8455 (2015).

[21] G. H. Vineyard, J. Phys. Chem. Solids **3**, 121 (1957).

[22] P. F. Bessarab, V. M. Uzdin, and H. Jónsson, Phys. Rev. B **85**, 184409 (2012).

[23] A. S. Varentcova, S. von Malottki, M. N. Potkina, G. Kwiatkowski, S. Heinze, and P. F. Bessarab, npj Comput. Mater. **6**, 193 (2020).

[24] A. S. Varentsova, M. N. Potkina, S. von Malottki, S. Heinze, and P. F. Bessarab, Nanosyst.: Phys. Chem. Math. **9**, 356 (2018).

[25] F. Muckel, S. von Malottki, C. Holl, B. Pestka, M. Pratzer, P. F. Bessarab, S. Heinze, and M. Morgenstern, Nat. Phys. **17**, 395 (2021).

[26] S. von Malottki, P. F. Bessarab, S. Haldar, A. Delin, and S. Heinze, Phys. Rev. B **99**, 060409(R) (2019).

[27] P.F. Bessarab, D. Yudin, D.R. Gulevich, P. Wadley, M. Titov, and O. A. Tretiakov, Phys. Rev. B **99**, 140411(R) (2019).

[28] L. Rózsa, E. Simon, K. Palotás, L. Udvardi, and L. Szunyogh, Phys. Rev. B **93**, 024417 (2016).

[29] M. Hoffmann, G. P. Müller, and S. Blügel, Phys. Rev. Lett. **124**, 247201 (2020).

[30] M. Potkina, I. Lobanov, H. Jónsson, and V. Uzdin, J. Magn. Magn. Mater., **5**49 168974 (2022).

[31] V. M. Uzdin, M. N. Potkina, I. S. Lobanov, P. F. Bessarab, and H. Jónsson, J. Magn. Magn. Mater. **459**, 236 (2018).

[32] M. Schott, A. Bernand-Mantel, L. Ranno, S. Pizzini, J. Vogel, H. Béa, C. Baraduc, S. Auffret, G. Gaudin, and D. Givord, Nano Lett. **17**, 3006 (2017).

[33] P.-J. Hsu, A. Kubetzka, A. Finco, N. Romming, K. von Bergmann, and R. Wiesendanger, Nat. Nanotechnol. **12**, 123 (2017).

[34] C.-G. Duan, J. P. Velev, R. F. Sabirianov, Z. Zhu, J. Chu, S. S. Jaswal, and E. Y. Tsymbal, Phys. Rev. Lett. **101**, 137201 (2008).

[35] F. Matsukura, Y. Tokura, and H. Ohno, Nat. Nanotechnol. **10**, 209 (2015).

[36] M. Oba, K. Nakamura, T. Akiyama, T. Ito, M. Weinert, and A. J. Freeman, Phys. Rev. Lett. **114**, 107202 (2015).

[37] H. Yang, O. Boulle, V. Cros, A. Fert, and M. Chshiev, Sci. Rep. **8**, 12356 (2018).

[38] L. Desplat, S. Meyer, J. Bouaziz, P.M. Buhl, S. Lounis, B. Dupé, and P.-A. Hervieux, Phys. Rev. B **104**, L060409 (2021).

[39] T. Srivastava, M. Schott, R. Juge, V. Krizakova, M. Belmeguenai, Y. Roussigné, A. Bernand-Mantel, L. Ranno, S. Pizzini, S.-M. Chérif *et al.*, Nano Lett. **18**, 4871 (2018).

[40] S. Paul and S. Heinze, npj Comput. Mater. **8**, 105 (2022).

[41] S. von Malottki, B. Dupé, P. Bessarab, A. Delin, and S. Heinze, Sci. Rep. **7**, 12299 (2017).

[42] M. Böttcher, S. Heinze, S. Egorov, J. Sinova, and B. Dupé, New J. Phys. **20**, 103014 (2018).

[43] P. Lindner, L. Bargsten, S. Kovarik, J. Friedlein, J. Harm, S. Krause, and R. Wiesendanger, Phys. Rev. B **101**, 214445 (2020).

[44] B. Heil, A. Rosch, and J. Masell, Phys. Rev. B **100**, 134424 (2019).

[45] S.-Z. Lin and S. Hayami, Phys. Rev. B **93**, 064430 (2016).

[46] B. Dupé, M. Hoffmann, C. Paillard, and S. Heinze, Nat. Commun. **5**, 4030 (2014).

[47] M. Hoffmann, Master thesis, Institute of Theoretical Physics and Astrophysics, University of Kiel, 2013

[48] J. Mentink, M. Tretyakov, A. Fasolino, M. Katsnelson, and T. Rasing, J. Phys.: Condens. Matter **22**, 176001 (2010).

[49] P. F. Bessarab, V. M. Uzdin, and H. Jónsson, Comput. Phys. Commun. **196**, 335 (2015).

[50] P. F. Bessarab, Phys. Rev. B **95**, 136401 (2017).

[51] J. Wild, T. N. Meier, S. Pöllath, M. Kronseder, A. Bauer, A. Chacon, M. Halder, M. Schowalter, A. Rosenauer, J. Zweck *et al.*, Sci. Adv. **3**, e1701704 (2017).

[52] G. Mills, H. Jónsson, and G. K. Schenter, Surf. Sci. **324**, 305 (1995).

[53] Note that the experimental lifetime has been measured at a bias voltage of $U = -0.6\,V$. This corresponds to an electric field of $\mathcal{E} = -U/d = 0.06$ to 0.12 V/Å in the plate capacitor approximation and assuming a tip-sample distance d of 5 to 10 Å. This amounts to a change of J_1 by at most 0.5% (cf. Table I), which has been neglected in this comparison.

[54] B. Dupé, G. Bihlmayer, M. Böttcher, S. Blügel, and S. Heinze, Nat. Commun. **7**, 11779 (2016).

[55] R. Toral and P. Colet, *Stochastic Numerical Methods: An Introduction for Students and Scientists* (John Wiley & Sons, Hoboken, NJ, 2014).